Available online at www.sciencedirect.com
ScienceDirect
Comput. Methods Appl. Mech. Engrg. 393 (2022) 114692
Computer methods in applied mechanics and engineering
www.elsevier.com/locate/cma

Moment method based distributed multipoles for modeling magnetic materials in 2D and 3D magnetostatics

Sangheon Lee, Hoyoung Kim, Hungsun Son*

Ulsan National Institute of Science and Technology, Ulsan, South Korea

Received 5 November 2021; received in revised form 28 January 2022; accepted 28 January 2022
Available online 8 March 2022

Abstract

This paper aims to develop a new modeling method, referred to as a moment method based distributed multipoles (MMDMP), for precise and fast computation of magnetic field and force involving various magnetic materials such as a permanent magnet (PM), an electromagnet (EM) and a ferromagnetic material (FM). The method decomposes the magnetic materials into local sources, consisting of volume and surface elements. Then, the magnetic field from the local sources is computed with the magnetization and demagnetization tensors of the elements. The demagnetization tensors are derived as a closed-form according to the geometry of the elements, which can be further converted into multipoles based on the distance between an observation point and the elements for computational efficiency. Additionally, the MMDMP is applied to the FM and EM by analyzing the magnetization of both materials due to existing magnetic fields. Magnetic interactions among the materials are computed by the sum of the elemental forces, which are forces on the local sources. The computational accuracy and efficiency are verified by field distribution and the force and torque interaction between the PM and an iron-core EM in 3D space. The results are compared to numerical solutions from a finite element method (FEM) and fundamental integral form equations such as Biot–Savart law. Finally, the MMDMP is applied to analyze the magnetic field of a brushless direct current (BLDC) motor and validated by the FEM and experiments. The results show that the MMDMP can provide fast and accurate analysis of magnetic characteristics of electromechanical systems.
© 2022 Elsevier B.V. All rights reserved.

Keywords: Electromagnetic analysis; Magnetostatics; Magnetic force; Permanent magnet motor; Magnetic multipoles modeling

1. Introduction

Computational methods of magnetostatics for magnetic materials, including permanent magnets (PMs), ferromagnetic materials (FMs), and electromagnets (EMs), have been studied for decades. They have played an essential role in analyzing magnetic characteristics of electromechanical systems such as magnetic saturation, the interactional force of electromechanical systems [1–6]. Most studies have relied on finite element methods (FEMs), which solve partial differential equations (PDEs) with given material information and magnetic boundary conditions. It is the most popular method because many commercial FEM tools are easily used with graphical user interfaces. However, it often requires fine and dense meshes along the boundaries of the materials to handle the boundary conditions at

* Corresponding author.
E-mail address: hson@unist.ac.kr (H. Son).

https://doi.org/10.1016/j.cma.2022.114692
0045-7825/© 2022 Elsevier B.V. All rights reserved.

surfaces of the materials. It could take substantial computational time and memory according to the complexity of the geometries of the materials. In addition, it requires modeling of the media regions, which can affect the convergence and accuracy of the solution. Consequently, it should be carefully handled to study moving magnetic sources that can change the geometry of media regions. In order to overcome the drawbacks of the FEM, several methods have been proposed to model the magnetic sources with coarse meshes. They can quickly provide a magnetic field and force computation for design optimization and control of PM and EM based actuators and sensors [7–9].

A magnetic dipole model has been applied for analyzing magnetic field for various applications. A distributed multipoles (DMP) method [7] provides a closed-form solution of the field and force of the PM. The method characterizes the PM as a set of monopoles and approximates the field of the PM as the sum of the field by poles. The location and strength of the poles are optimized by a known reference field which can be computed analytically or by the FEM with the given magnetization field of the PM. In [10], the DMP method is applied to a cylindrical multilayer EM which can be converted to a cylindrical PM by an equivalent magnetization. In [11], the magnetization of a soft iron object is analyzed using an image method that reflects poles of magnets beneath the surface of the soft iron. The DMP method has a significant advantage in fast calculation and visualization of the magnetic field because it is unnecessary to model the media region. In addition, the interaction between magnetic materials is computed by the sum of interaction between poles, expressed the final solution as a closed-form. However, the DMP method depends on the other computational methods to utilize the reference field. In addition, it has limitations in modeling the internal field of materials, the EMs of various shapes, and the FMs with complex geometry. Nevertheless, due to its computational effectiveness, it has been used in lots of practical applications, such as an orientation sensor [12], spherical wheel motor [13,14], and magnetic induction tomography [15].

A distributed current sources (DCS) method [8] has been studied to overcome the limitation of the DMP method. It utilizes the conceptual surface current which characterizes the magnetization of PM. Furthermore, the surface current of linear FM can be determined based on the boundary conditions. Therefore, all the materials are modeled as distributed point current sources. It does not require any reference field data, but it recursively decomposes a single point source into a set of local sources. The decomposition level of each point source is adjusted by the distance between a point source and an observation point. Thus, the distribution of the local sources could change according to the observation point so that it may have inefficiency in memory management. In addition, the magnetostatic analysis of the FM is limited to the linear material. Nonetheless, the model utilizes physical currents flowing, so it has been widely used in practical applications to analyze eddy current distribution [16–19].

Similarly, a moment method (MM) approximates the magnetic source to a set of uniformly magnetized volume elements. It does not require modeling the media region same as the DMP and the DCS. Besides, it does not need to consider the boundary condition, unlike numerical methods. Thus, it is relatively easy to formulate inverse problems than conventional FEM [20,21]. In addition, the magnetization of the FM can be found iteratively with its nonlinear characteristics [9,22]. However, the MM requires integral computation for calculating the stray and demagnetization field of each volume element. This computational load can be reduced with the aid of the demagnetization tensor of each mesh, which has been studied for several geometries, a rectangular prism [23], an equilateral triangular prism [24], and a tetrahedron [25]. Nonetheless, integral computations are still necessary for calculating the interaction force, expressed by the Maxwell stress tensor or the Lorentz force, and the magnetic field by the free current, expressed by the Biot–Savart law. Furthermore, the research on demagnetization tensors of planar meshes is paid less attention to, so the development of planar models may be limited.

This paper develops a generalized source model referred to as a moment method based distributed multipoles (MMDMP), which can approximate the magnetic material as a set of the local sources. The MMDMP can provide the solutions without any numerical integration. The remainder of the paper is organized as follows:

- The MMDMP decomposes the magnetic materials into local sources, which can be volume or surface elements according to the types of materials. The magnetic field generated by the elements is computed by the demagnetization tensors expressed as closed-forms. Next, the elements can be further approximated as either monopoles or dipoles based on the distance to an observation point to reduce the efforts in computing the tensor.
- The MMDMP is applied to characterize the magnetization field and interaction force of the FM and EM. The induced magnetization field in the nonlinear FMs is computed by an iterative method which can account for the nonlinear BH curve of the materials. The linear FM is further modeled by surface elements, and their magnetization can be found by a linear system. Next, the equivalent magnetization of the EM in [10] is

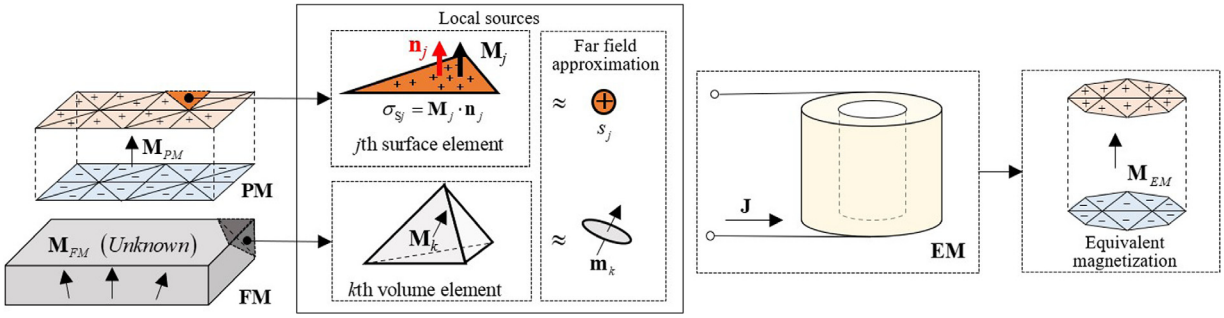


Fig. 1. PM, FM, and EM models and local sources in the MMDMP.

generalized to the multilayer EMs of various shapes. Lastly, the elemental forces applied to the local sources are derived as a closed-form and utilized to express the force and torque of the magnetic materials by summing the elemental forces.

– The computational advantages of the MMDMP are illustrated by two examples generally utilized for the electromechanical systems in practice; 1. Interaction between a moving PM and an iron-core EM in 3D space. 2. Analysis of a BLDC motor in 2D space. As will be shown, the method is as accurate as numerical solutions of fundamental integral form equations and more efficient than commercial FEM methods.

2. Moment method based distributed multipoles

2.1. Governing equation

Fig. 1 shows the conceptual model of the MMDMP for three different magnetic materials, PM, FM, and EM. A magnetization $\mathbf{M}$ is commonly used in magnetostatics. However, each model has a different characteristic of the magnetization $\mathbf{M}$. First, the magnetization of the PM, $\mathbf{M}_{\mathrm{PM}}$, is generally assumed to be constant as $\mathbf{M}_{\mathrm{PM}} = \mu_0^{-1}\mathbf{B}_{\mathrm{rem}}$ where μ_0 is the permeability of air and $\mathbf{B}_{\mathrm{rem}}$, measurable remanence field of the PM. The constant magnetization distributes the magnetic charges on the surfaces of the PM. Second, the magnetization of the FM, $\mathbf{M}_{\mathrm{FM}}$, can vary according to the applied field and its BH curve. Hence, $\mathbf{M}_{\mathrm{FM}}$ is generally non-uniform, unlike the PM. Lastly, the EM can be equivalently characterized to the PM with magnetization $\mathbf{M}_{\mathrm{EM}}$, varying with a volume current density $\mathbf{J}$.

The MMDMP begins with the analysis of the magnetic field intensity $\mathbf{H}$ in (1) and (2), expressed as an equivalent form of (1), with a fictitious magnetic volume charge density $\sigma_{\mathrm{V}} = \nabla \cdot \mathbf{M}$ and a surface charge density $\sigma_{\mathrm{S}} = \mathbf{M}\cdot\mathbf{n}$ where $\mathbf{n}$ is a normal vector of the surface at $\mathbf{r}'$. In particular, σ_{V} vanishes in a special case, such as conventional PMs, since $\mathbf{M}_{\mathrm{PM}}$ is assumed to be uniform. The magnetic flux density $\mathbf{B}$ at $\mathbf{r}$ with the aid of given $\mathbf{M}$. [26]

$$\mathbf{H}(\mathbf{r}) = \frac{1}{4\pi}\int_{V'} 3\left|\boldsymbol{\rho}\right|^{-5}\left(\mathbf{M}\cdot\boldsymbol{\rho}\right)\boldsymbol{\rho} - \left|\boldsymbol{\rho}\right|^{-3}\mathbf{M}dV' \tag{1}$$

$$= \frac{1}{4\pi}\left\{\int_{V'}\boldsymbol{\rho}\left|\boldsymbol{\rho}\right|^{-3}\sigma_{\mathrm{V}}dV' + \int_{S'}\boldsymbol{\rho}\left|\boldsymbol{\rho}\right|^{-3}\sigma_{\mathrm{S}}dS'\right\} \tag{2}$$

$$\mathbf{B}(\mathbf{r}) = \mu_0\left(\mathbf{H}(\mathbf{r}) + \mathbf{M}(\mathbf{r})\right) \tag{3}$$

where $\boldsymbol{\rho} = \mathbf{r} - \mathbf{r}'$ and dV' is an infinitesimal volume with respect to $\mathbf{r}'$; dS' is an infinitesimal surface on a surface of the magnetic material.

The MMDMP characterizes magnetic materials as sets of surface and volume elements. Each surface element has a uniform σ_{S}, and each volume element is uniformly magnetized. As a result, $\mathbf{H}$ can be computed by summing all the contributions of the elements in (4).

$$\mathbf{H}(\mathbf{r}) = \sum_{j=1}^{n_S}\mathbf{H}_{Sj} + \sum_{k=1}^{n_V}\mathbf{H}_{Vk} \tag{4}$$

$$\mathbf{H}_{\mathrm{S}j}(\mathbf{r}) = \frac{1}{4\pi}\int_{S_j} \boldsymbol{\rho}_j \left|\boldsymbol{\rho}_j\right|^{-3} \sigma_{\mathrm{S}j} dS_j = \mathbf{N}_{\mathrm{S}j}\mathbf{M}_j \tag{5}$$

$$\mathbf{H}_{\mathrm{V}k}(\mathbf{r}) = \frac{1}{4\pi}\int_{V_k} 3\left|\boldsymbol{\rho}_k\right|^{-5}\left(\mathbf{M}_k\cdot\boldsymbol{\rho}_k\right)\boldsymbol{\rho}_k - \left|\boldsymbol{\rho}_k\right|^{-3}\mathbf{M}_k dV_k = \frac{1}{4\pi}\int_{S_k} \boldsymbol{\rho}_k \left|\boldsymbol{\rho}_k\right|^{-3}\sigma_{\mathrm{S}k} dS_k = \mathbf{N}_{\mathrm{V}k}\mathbf{M}_k \tag{6}$$

where $\mathbf{H}_{\mathrm{S}j}$ and $\mathbf{H}_{\mathrm{V}k}$ represent the contribution of the jth surface and kth volume element, respectively. n_{S} and n_V are the numbers of the surface and volume elements. $\boldsymbol{\rho}_j = \mathbf{r} - \mathbf{r}_j$, where $\mathbf{r}_j$ is the barycenter of the jth local source. In (5), $\mathbf{H}_{\mathrm{S}j}$ is expressed by the surface charge density $\sigma_{\mathrm{S}j} = \mathbf{M}_j \cdot\mathbf{n}_j$ and the area of the element S_j, where $\mathbf{M}_j = \mathbf{M}(\mathbf{r}_j)$ represents the magnetization of the jth local source. The surface integral in (5) can be further expressed by multiplying a demagnetization tensor $\mathbf{N}_{\mathrm{S}j}$ and $\mathbf{M}_j$. $\mathbf{M}_k$ and V_k in (6) are the magnetization and the volume of the kth volume element. Its uniform magnetization vanishes σ_{V}. In other words, $\mathbf{H}_{\mathrm{V}k}$ can be described by summing the effect of surfaces of the volume element. Therefore, it is expressed by its demagnetization tensor $\mathbf{N}_{\mathrm{V}k}$, similar to (5).

2.2. Demagnetization tensor

The magnetic field intensity $\mathbf{H}$ in (4) can reduce the computational time compared to conventional FEM [20]. However, it still requires substantial computational efforts due to integrals in (5) and (6), which can be computed numerically. Therefore, it is better to express the demagnetization tensor in a closed-form for computational efficiency.

Fig. 2 shows a skinny rectangle and an infinitely long triangular prism for a surface and volume element in a 2D model, respectively. Three rectangles contribute to the magnetic field of the prism, so the demagnetization tensor of the rectangle is fundamental to compute the magnetic field. For the simplicity, a rectangle with vertices $\mathbf{A}^{\pm}(-l,\ 0,\ \pm\infty)$, $\mathbf{B}^{\pm}(l,\ 0,\ \pm\infty)$ is considered where $\mathbf{M} = M_y\mathbf{e}_y = -M_y\mathbf{n}$. Then, a demagnetization factor N_{xy} is derived to compute the x-component of $\mathbf{H} = H_x\mathbf{e}_x + H_y\mathbf{e}_y + H_z\mathbf{e}_z$ at $\mathbf{r} = x\mathbf{e}_x + y\mathbf{e}_y + z\mathbf{e}_z$.

$$H_x = \frac{M_y}{4\pi}\int_{-\infty}^{\infty}\int_{-l}^{l} \frac{-\left(x-x'\right)}{\left\{(x-x')^2 + (y)^2 + (z')^2\right\}^{3/2}} dx'dz' = N_{xy}M_y \tag{7}$$

$$N_{xy} = -\frac{1}{4\pi}\ln\frac{(l+x)^2 + y^2}{(l-x)^2 + y^2} \tag{8}$$

Similarly, N_{yy} can be derived to compute H_y:

$$H_y = \frac{M_y}{4\pi}\int_{-\infty}^{\infty}\int_{-l}^{l} \frac{-y}{\left\{(x-x')^2 + (y)^2 + (z')^2\right\}^{3/2}} dx'dz' = N_{yy}M_y \tag{9}$$

$$N_{yy} = \begin{cases} 0\,(y=0) \\ -\frac{1}{2\pi}\left\{\arctan\left(\frac{l+x}{y}\right) + \arctan\left(\frac{l-x}{y}\right)\right\}\,(y\neq 0) \end{cases}. \tag{10}$$

H_z is neglected due to the symmetry of the rectangle about the xy plane. i.e. $N_{zy} = 0$.

The demagnetization tensor can be generalized to the arbitrary positioned and oriented rectangle. $\mathbf{N}_{\mathrm{S}j}$ is expressed for the jth rectangle in (11) with the coordinate transform matrix in (12).

$$\mathbf{N}_{\mathrm{S}j}(\mathbf{r}) = \mathbf{P}_j\mathbf{N}_{\mathrm{P}}\left(\mathbf{P}_j^T\mathbf{r} - \mathbf{P}_j^T\mathbf{D}_j\right)\mathbf{P}_j^T \tag{11}$$

$$\mathbf{P}_j = \begin{bmatrix} \mathbf{e}_{xj} & \mathbf{e}_{yj} & \mathbf{e}_{zj} \end{bmatrix} \tag{12}$$

where $\mathbf{N}_{\mathrm{P}}(\mathbf{r}) = [0\ N_{xy}\ 0;\ 0\ N_{yy}\ 0;0\ N_{zy}\ 0]$. $\mathbf{D}_j$ is the center of the rectangle and $\mathbf{P}_j$ represents the local coordinate of the rectangle in terms of a global coordinate $\{\mathbf{G}\}$.

Meanwhile, $\mathbf{H}_{\mathrm{V}k}$ by the kth prism can be expressed as $\mathbf{H}_{\mathrm{V}k} = \mathbf{N}_{S1}\mathbf{M}_k + \mathbf{N}_{S2}\mathbf{M}_k + \mathbf{N}_{S3}\mathbf{M}_k$ by (6), where $\mathbf{N}_{Sj}$ is the tensor of the jth rectangle making up the prism. As a result, the demagnetization tensor $\mathbf{N}_{Vk}$ in (6) can be expressed in (13).

$$\mathbf{N}_{\mathrm{V}k}(\mathbf{r}) = \sum_{j=1}^{3}\mathbf{N}_{\mathrm{S}j} \tag{13}$$

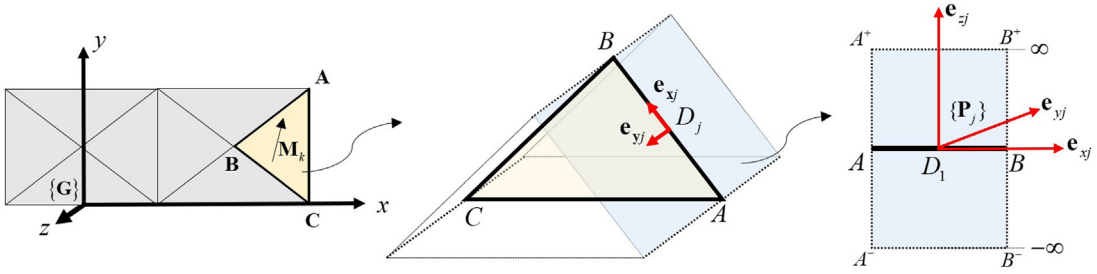


Fig. 2. Surface and volume elements for 2D model.

In addition, (13) is not limited to a triangular prism but can be extended to any prism by adding the tensors of rectangles.

As a result, (4) can be simplified as (14) with the aid of the tensors.

$$\mathbf{H} = \sum_{k=1}^{n_S} \mathbf{N}_{Sj}\mathbf{M}_j + \sum_{k=1}^{n_V} \mathbf{N}_{Vk}\mathbf{M}_k \tag{14}$$

Furthermore, a triangle and tetrahedral element can be considered for a 3D model. Similar to (7)–(12), the tensor of the triangle can be derived. Then, the tensor of the tetrahedron is computed by the contributions of four triangles making up the tetrahedron [25].

2.3. Distributed multipoles

Demagnetization tensors must be updated for every observation point. It still takes a heavy computational load to compute (14). This limitation can be overcome by approximating the surface and volume element as monopole and dipole for far-field observation, respectively.

Dipole approximation

The volume element of the 2D model is an infinitely long prism. Therefore, the magnetic field can be computed in (15) since an infinite line of dipoles approximates the element.

$$\mathbf{H}_{Vk} = \begin{cases} \mathbf{N}_{Vk}\mathbf{M}_k \left(\left|\boldsymbol{\rho}_{ik}\right| \le \varepsilon_k\right) \\ \frac{1}{2\pi\left|\boldsymbol{\rho}_k\right|^2}\left(\frac{2\underline{\mathbf{m}}_k\cdot\boldsymbol{\rho}_k}{\left|\boldsymbol{\rho}_k\right|^2}\boldsymbol{\rho}_k - \underline{\mathbf{m}}_k\right)\left(\left|\boldsymbol{\rho}_k\right| > \varepsilon_k\right) \end{cases} \tag{15}$$

where $\underline{\mathbf{m}}_k = A_k\mathbf{M}_k$ represents a total dipole moment per unit length carried by the element and A_k is an area of the base of the kth prism. The criterion ε_k can be determined according to the size of the element.

Similarly, the kth volume element in the 3D model is uniformly magnetized with a total dipole moment $\mathbf{m}_k = V_k\mathbf{M}_k$. Therefore, if $|\boldsymbol{\rho}_k| > \varepsilon_k$, a single dipole approximates the element as expressed in (16).

$$\mathbf{H}_{Vk} = \begin{cases} \mathbf{N}_{Vk}\mathbf{M}_k \left(\left|\boldsymbol{\rho}_k\right| \le \varepsilon_k\right) \\ \frac{1}{4\pi\left|\boldsymbol{\rho}_k\right|^3}\left(\frac{3\mathbf{m}_k\cdot\boldsymbol{\rho}_k}{\left|\boldsymbol{\rho}_k\right|^2}\boldsymbol{\rho}_k - \mathbf{m}_k\right)\left(\left|\boldsymbol{\rho}_k\right| > \varepsilon_k\right) \end{cases} \tag{16}$$

Monopole approximation

The surface in the 2D model is an infinitely long rectangle which can be modeled as an infinite line of monopole:

$$\mathbf{H}_{Sj} = \begin{cases} \mathbf{N}_{Sj}\mathbf{M}_j \left(\left|\boldsymbol{\rho}_j\right| \le \varepsilon_j\right) \\ \frac{\underline{s}_j}{2\pi\left|\boldsymbol{\rho}_j\right|^2}\boldsymbol{\rho}_j \left(\left|\boldsymbol{\rho}_j\right| > \varepsilon_j\right) \end{cases} \tag{17}$$

where $\underline{s}_j = w_j\sigma_{Sj}$ represents the strength of the pole per unit length on the jth rectangle and w_j is the width of the rectangle.

In the 3D model, the surface element is full of magnetic charges with the charge density σ_{Sj}. Therefore, it carries the charge amount of $s_j = S_j\sigma_{Sj}$, so a monopole can approximate the element as expressed in (18).

$$\mathbf{H}_{Sj} = \begin{cases} \mathbf{N}_{Sj}\mathbf{M}_j \left(\left|\boldsymbol{\rho}_j\right| \le \varepsilon_j\right) \\ \frac{s_j}{4\pi\left|\boldsymbol{\rho}_j\right|^3}\boldsymbol{\rho}_j \left(\left|\boldsymbol{\rho}_j\right| > \varepsilon_j\right) \end{cases} \tag{18}$$

As a result, magnetic materials can be modeled with distributed local sources, consisting of monopoles, dipoles, and surface and volume elements. The local sources can be configured depending on where the magnetic field is observed. For example, if the observation point is exceptionally far from a material, the material is modeled as distributed multipoles. Conversely, if the field is observed extremely close to the material, it is better to utilize surface and volume elements as well.

2.4. Magnetization of FM object and EM

The magnetization of the materials is required in (14), but it is difficult to identify for the FM and EM. The magnetization of the FM changes according to the applied magnetic field, while the PM almost keeps uniform magnetization. The magnetization of the FM is difficult to analyze due to its nonlinear characteristics. Unlike the FM and PM, the EM has no physical magnetic dipole indicating magnetization, although their current loops act like dipoles. Thus, it is important but challenging to analyze the magnetization of the FM and EM for a generalized magnetic source model.

Ferromagnetic material

Magnetization of an isotropic FM has a nonlinear relationship with $\mathbf{H}$ expressed as

$$\mathbf{M} = \chi\mathbf{H} \tag{19}$$

$$\chi = f\left(|\mathbf{H}|\right) \tag{20}$$

where χ is a magnetic susceptibility. According to (14) and (19), $\mathbf{H}$ at the barycenter of each volume element $\mathbf{H}_i = \mathbf{H}(\mathbf{r}_i)$ can be expressed as

$$\mathbf{H}_i = \mathbf{H}_{0i} + \sum_{k=1}^{n_V} \mathbf{N}_{Vik}\mathbf{M}_k = \chi_i^{-1}\mathbf{M}_i \tag{21}$$

where $\mathbf{N}_{Vik} = \mathbf{N}_{Vk}(\mathbf{r}_i)$ and $\mathbf{H}_{0i}$ is applied magnetic field by other magnetic materials at $\mathbf{r} = \mathbf{r}_i$.

Furthermore, (21) can be formulated as a linear system in (22).

$$\left(\boldsymbol{\Gamma}\left([\mathbf{H}_k]_{n_V}\right) - \mathbf{N}_V\right)[\mathbf{M}_k]_{n_V} = [\mathbf{H}_{0k}]_{n_V} \tag{22}$$

where $[\ ]_n$ combines n column vectors into a single column vector. For example, $[\mathbf{H}_k]_n = [\mathbf{H}_1; \mathbf{H}_2; \cdots; \mathbf{H}_n]$. $\mathbf{N}_V$, consisting of $\mathbf{N}_{Vik}$, is a $3n_V \times 3n_V$ matrix for the 3D model. $\boldsymbol{\Gamma}([\mathbf{H}_k]_n)$ is an inverse susceptibility matrix. If the material is linear, $\boldsymbol{\Gamma} = \chi^{-1}\mathbf{I}$ where χ is a constant and $\mathbf{I}$ is the identity matrix. In this case, (22) can be solved by a matrix inversion. However, the nonlinear susceptibility is coupled with the applied magnetic field by (20). Therefore, it is impossible to solve (22) by the matrix inversion. Thus, (23)–(25) are introduced to determine the susceptibility of each element iteratively.

$$[\mathbf{M}_k]_{n_V}^{(q+1)} = \left(\boldsymbol{\Gamma}\left([\mathbf{H}_k]_{n_V}^{(q)}\right) - \mathbf{N}_V\right)^{-1}[\mathbf{H}_{0k}]_{n_V} \tag{23}$$

$$[\mathbf{H}]_{n_V}^{(q+1)} = [\mathbf{H}_0]_{n_V} + \mathbf{N}_V[\mathbf{M}]_{n_V}^{(q+1)} \tag{24}$$

$$\chi_k^{(q+1)} = f\left(\left|\mathbf{H}_k^{(q+1)}\right|\right) \tag{25}$$

where the superscript q represents the qth iteration step. The iteration stops when the susceptibility of every element is converged. The initial value can be set as $[\mathbf{H}_k]_{n_V}^{(0)} = [\mathbf{H}_{0k}]_{n_V}$.

The magnetic field interaction in (22), utilizing volume elements, can be applied to the linear FM. However, surface elements can also model the linear FM because linear susceptibility vanishes σ_V. Thus, only the normal components of the magnetization can modify the surface charge density of the elements and be determined to satisfy a boundary condition, $B_{\mathrm{n}i}^{+} = B_{\mathrm{n}i}^{-}$, where $B_{\mathrm{n}i}$ represents the normal component of the magnetic field $\mathbf{B}_i = \mathbf{B}(\mathbf{r}_i)$. The superscript $\pm$ means the physical quantities at $\mathbf{r}= \mathbf{r}_i \pm \varepsilon \mathbf{n}_i$ and $\varepsilon \rightarrow 0+$, where $\mathbf{n}_i$ is the normal vector of the ith surface element. Based on (3) and (19), the boundary condition is expressed by the normal component of $\mathbf{H}_i$ as $H_{\mathrm{n}i}^{+} = (\chi + 1) H_{\mathrm{n}i}^{-}$, assuming the media region outside the FM is the air. Finally, it is formulated as (26) according to (14).

$$H_{0\mathrm{n}i}^{+} + \sum_{j=1}^{n_S} \left(\mathbf{N}_{\mathrm{S}ij}^{+} \mathbf{M}_{\mathrm{n}j} \right) \cdot \mathbf{n}_i = \mu_r \left\{ H_{0\mathrm{n}i}^{-} + \sum_{j=1}^{n_S} \left(\mathbf{N}_{\mathrm{S}ij}^{-} \mathbf{M}_{\mathrm{n}j} \right) \cdot \mathbf{n}_i \right\} \tag{26}$$

where $\mu_r = \chi + 1$ is a relative permeability and $\mathbf{N}_{\mathrm{S}ij} = \mathbf{N}_{\mathrm{S}j}(\mathbf{r}_i)$. The normal component of the magnetization of the jth element $\mathbf{M}_{\mathrm{n}j} = M_{\mathrm{n}j} \mathbf{n}_j$. $H_{0\mathrm{n}j}$ represents the normal component of $\mathbf{H}_{0j}$.

In addition, $B_{\mathrm{n}i}^{-} = \mu_0 (H_{\mathrm{n}i}^{-} + M_{\mathrm{n}i})$, according to (3). Thus, the boundary condition also can be formulated as

$$H_{0\mathrm{n}i}^{+} + \sum_{j=1}^{n_S} M_{\mathrm{n}j} \left(\mathbf{N}_{\mathrm{S}ij}^{+} \mathbf{n}_j \right) \cdot \mathbf{n}_i = H_{0\mathrm{n}i}^{-} + \sum_{j=1}^{n_S} M_{\mathrm{n}j} \left(\mathbf{N}_{\mathrm{S}ij}^{-} \mathbf{n}_j \right) \cdot \mathbf{n}_i + M_{\mathrm{n}i} \tag{27}$$

By combining (26) and (27), the normal component of the applied field can be expressed in terms of the magnetization as

$$H_{0\mathrm{n}i}^{-} = \chi^{-1} M_{\mathrm{n}i} - \sum_{j=1}^{n_S} M_{\mathrm{n}j} \left(\mathbf{N}_{\mathrm{S}ij}^{-} \mathbf{n}_j \right) \cdot \mathbf{n}_i \tag{28}$$

As a result, M_{nj} can be found by solving linear Eq. (29).

$$\left(\chi^{-1} \mathbf{I} - \mathbf{N}_{\mathrm{S}} \right) \left[M_{\mathrm{n}j} \right]_{n_S} = \left[H_{0\mathrm{n}j}^{-} \right]_{n_S} \tag{29}$$

where $\mathbf{N}_{\mathrm{S}}$, consisting of $(\mathbf{N}_{\mathrm{S}ij}^{-} \mathbf{n}_j) \cdot \mathbf{n}_i$, is $n_S \times n_S$ matrix.

Surface elements can be more efficient than volume elements in modeling the linear FM because the surface generally requires fewer meshes than the entire volume. In addition, (29) is more expeditious than (22) to get inverse matrix even in $n_{\mathrm{S}} = n_{\mathrm{V}}$, considering the dimension of $\mathbf{N}_{\mathrm{V}}$ in (22) is $3n_V \times 3n_V$ for the 3D model.

Electromagnet

An EM can be designed with various shapes and controllable strengths of the field. Generally, it can be analyzed by the Biot–Savart law utilizing the volume integral along with an input current directly, which often requires heavy computation. The MMDMP converts the EM into the equivalent PM to utilize (14) instead of the Biot–Savart law. A multilayer EM with a cuboid core can be considered, as shown in Fig. 3. The equivalent magnetization $\mathbf{M}_{EM} = M \hat{\mathbf{e}}_z$ is defined by the input current to characterize the EM as the PM, where $\hat{\mathbf{e}}_z$ represents the axis of the EM. $\mathbf{M}_{EM}$ generates the magnetization currents (30)–(31), equivalent to the actual input current of the EM.

$$\lim_{\varepsilon \rightarrow 0+} \left(\mathbf{M}_{EM} \left(\mathbf{r} + \varepsilon \hat{\mathbf{e}}_n \right) \times \hat{\mathbf{e}}_n + \mathbf{M}_{EM} \left(\mathbf{r} - \varepsilon \hat{\mathbf{e}}_n \right) \times \left(-\hat{\mathbf{e}}_n \right) \right) = \mathbf{J}_S = 0 \tag{30}$$

$$\nabla \times \mathbf{M}_{EM}(\mathbf{r}) = \frac{\partial M}{\partial t} \hat{\mathbf{e}}_n - \frac{\partial M}{\partial n} \hat{\mathbf{e}}_t = \mathbf{J}_V = \begin{cases} J \hat{\mathbf{e}}_t \ (\mathbf{r} \in C_2) \\ 0 \ (\mathbf{r} \in C_1 \cup C_3) \end{cases} \tag{31}$$

$\mathbf{r} = n \hat{\mathbf{e}}_n + t \hat{\mathbf{e}}_t + z \hat{\mathbf{e}}_z$; $\hat{\mathbf{e}}_t$ is a direction of the current flow at $\mathbf{r}$ and $\hat{\mathbf{e}}_n = \hat{\mathbf{e}}_t \times \hat{\mathbf{e}}_z$. The volume current density of the EM $\mathbf{J}_V = J \hat{\mathbf{e}}_{\mathrm{t}}$. $C_1 \sim C_3$ are domains defined in Fig. 3.

The magnetization M depends on n but not t to hold (31). Also, $\mathbf{M}_{EM}$ is continuous in all domains to make surface current density $\mathbf{J}_S$ zero in (30). Consequently, M can be derived as

$$M = \begin{cases} M_1 = J w \ (\mathbf{r} \in C_1) \\ M_2 - J n = J \left(n_o - n \right) \ (\mathbf{r} \in C_2) \\ 0 \ (\mathbf{r} \in C_3) \end{cases} \tag{32}$$

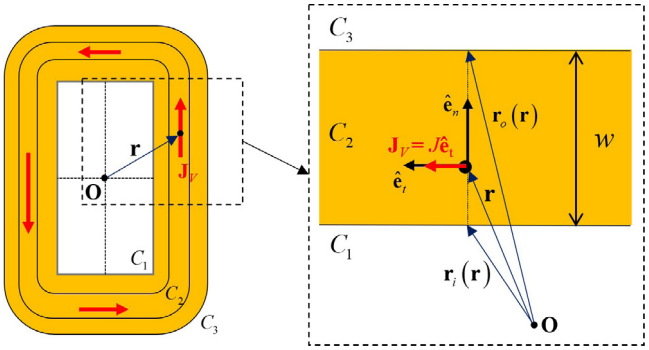


Fig. 3. Coordinate system of a multilayer EM.

where w is the thickness of the multilayer. n_o is the normal component of $\mathbf{r}_o$, which is the projection of $\mathbf{r}$ onto the outer surface of the EM. Without loss of generality, (32) can be applied to various core shapes, such as cylinders.

2.5. Force and torque model

Magnetic force and torque can be expressed as a sum of the elemental force $\mathbf{F}_k$ and torque $\mathbf{T}_k$, acting on the kth element by the applied field $\mathbf{H}_0$. $\mathbf{F}_k$ and $\mathbf{T}_k$ are formulated differently according to the types of the kth element. It is assumed that the barycentric interpolation can represent $\mathbf{H}_0$ over the kth elements.

The force acting on the volume element can be expressed in (33). The barycentric interpolation of $\mathbf{H}_0$ makes the gradient of $\mathbf{M}_k \cdot \mathbf{H}_0$ uniform. As a result, $\mathbf{F}_k$ is simplified as (34).

$$\mathbf{F}_k = \mu_0 \int \nabla \left(\mathbf{M}_k \cdot \mathbf{H}_0\right) dV_k \tag{33}$$

$$\mathbf{F}_k = \mu_0 \nabla \left(\mathbf{m}_k \cdot \mathbf{H}_0\right) \tag{34}$$

where the gradient in (34) can be calculated with $\mathbf{H}_0$ at each node of the kth element.

Similarly, torque about the origin $\mathbf{T}_k$ can be derived in (35). It consists of the torque by $\mathbf{F}_k$ and the moment to align the dipole moment to $\mathbf{H}_0$.

$$\mathbf{T}_k = \mathbf{r}_k \times \mathbf{F}_k + \mu_0 \int \mathbf{M}_k \times \mathbf{H}_0 dV_k \tag{35}$$

where the second term is equivalent to $\mu_0 \mathbf{m}_k \times \mathbf{H}_0$ by the barycentric interpolation. Consequently, $\mathbf{T}_k$ is simplified as (36).

$$\mathbf{T}_k = \mathbf{r}_k \times \mathbf{F}_k + \mu_0 \mathbf{m}_k \times \mathbf{H}_{0k} \tag{36}$$

where $\mathbf{H}_{0k}$ is the applied field at $\mathbf{r} = \mathbf{r}_k$.

The force acting on the kth surface element can be derived as (37). It is simplified as (38) by the barycentric interpolation and utilized to compute the elemental torque $\mathbf{T}_k = \mathbf{r}_k \times \mathbf{F}_k$.

$$\mathbf{F}_k = \mu_0 \int \sigma_{Sk} \mathbf{H} dS_k \tag{37}$$

$$\mathbf{F}_k = \mu_0 s_k \mathbf{H}_k \tag{38}$$

The magnetic force and torque can be computed without any numerical integration because $\mathbf{F}_k$ and $\mathbf{T}_k$ are obtained in the closed-form with the aid of $\mathbf{H}_0$ which can be calculated using (15)–(18).

3. Modeling example

Two practical applications illustrate the performance of accuracy and computational efficiency of the MMDMP. The first demonstrates the interaction between a moving PM and an iron-core EM in 3D space. Three different

Table 1
Properties of the PM and EM.

PM			
Width/Depth/Height	8.5/15/3 mm	Remanence (B_{rem})	1.42T
EM			
Core width($2a$)/depth($2b$)/height(h)	4/15/13 mm	Nonlinear core material	Silicon steel NGO 35PN250
Thickness of multilayer	1.75 mm	Number of turns	115

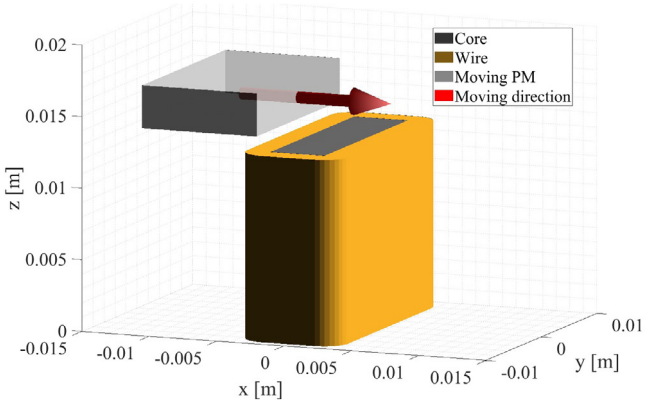


Fig. 4. Schematics of moving PM and iron-core EM.

magnetic properties are described to validate the model of each magnetic material and the interaction force. (1) The magnetic field of the air-core EM. (2) The magnetic field and magnetization of the EM with nonlinear iron-core. (3) Interaction force between moving PM and EM with nonlinear/linear iron-core. In the second, the field distribution and torque of a brushless direct current (BLDC) motor are investigated with a three-phase current input in 2D space.

3.1. Moving PM and iron-core EM

Fig. 4 shows an illustrative example with a moving PM and an EM. The MMDMP is applied to characterize various materials, PM and multilayer EM with air/iron core. For the far-field approximation, ε_k in (16) and (18) are set as $4{\cdot}max(|\mathbf{V}_{ki} - \mathbf{r}_k|)$ where $\mathbf{V}_{ki}$ represents the ith vertex of the kth local source. The geometric and magnetic properties of the sources are detailed in Table 1. The computational efficiency and accuracy results are compared to the numerical integration of governing equations and a commercial FEM software COMSOL.

Air-core EM

The air-core EM is modeled by surface elements. Its magnetization in (32) provides $\mathbf{M}_{\mathrm{EM}} = JM\mathbf{e}_z$ and M can be expressed in (39)

$$M = \begin{cases} R_I : w \\ R_{II} : w - (|y| - b) \\ R_{III} : w - (|x| - a) \\ R_{IV} : w - \sqrt{(|x| - a)^2 + (|y| - b)^2} \\ R_V : 0 \end{cases} \tag{39}$$

where $R_I \sim R_V$ are regions at the end of the EM and separated as shown in Fig. 5(a). The volume current density J is assumed to be homogeneous, so it is computed by the number of turns N and current I as $J = NI/(wh)$. Geometric parameters w, a, b, and h are given in Table 1. Fig. 5(b) represents the magnetization of each surface element at both ends of the EM.

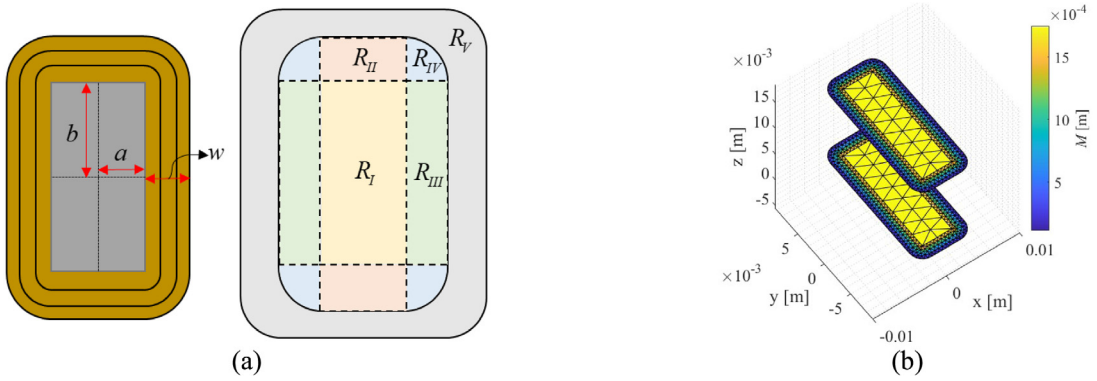


Fig. 5. Magnetization of the air-core EM.

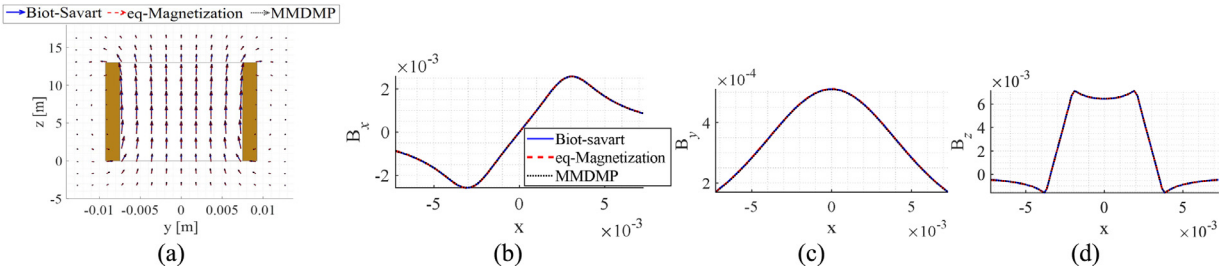


Fig. 6. B field by the air-core EM with 1 A (a) **B** at $x = 0$ (b–d) $B_x \sim B_z$ at $y = b/2$ and $z = h + 1$ mm.

Table 2
Comparison of computation methods in Fig. 6(b–d).

Average computational time [s]			
Biot–Savart Law	(2) with equivalent magnetization		MMDMP
1.967	0.0635		0.0056
Average computational error[a] [%]	B_x	B_y	B_z
(2) with equivalent Magnetization	0.0023	0.0005	0.0028
MMDMP	0.0714	0.0160	0.0542

[a]Average computational error of an element of vector $\boldsymbol{v} = mean((\boldsymbol{v}_i - \boldsymbol{v}_{ref,i})/max|\boldsymbol{v}_{ref}|)(i = x \sim z)$ where $\boldsymbol{v}_{ref}$ represents a base solution.

Fig. 6 illustrates the **B** field computed by three methods; Numerical integration of the Biot–Savart law and (2) with the equivalent magnetization (39), and the MMDMP. In the MMDMP, the EM is modeled by surface elements. The computation results are shown in Fig. 6(b)–(d) and compared quantitatively at the field at $y = b/2$ and $z = h - 1$ mm. The integration of (2) shows excellent accuracy with less than 0.01% error based on the numerical integration of the Biot–Savart law. The results verify that (32) can represent the physics of the multilayer EM. In addition, it requires the surface integral, while the Biot–Savart law requires the volume integral. Therefore, it could save computational time by reducing the domain of the numerical integration. Furthermore, the MMDMP shows the fastest computational speed because the field is computed by summing the closed-form solutions without numerical integration. The results of the MMDMP still are in excellent agreement with the other methods (see Table 2).

Iron-core EM

The iron-core EM is modeled with volume elements. Its magnetization $\mathbf{M}_{\mathrm{FM}}$ is calculated by iterating (23)–(25) with the applied field by the surface elements of the air-core EM. The MH curve of the silicon steel NGO 35PN250, in Fig. 7(a), is used in (25). The curve is generated by linear curve fitting to markers, the BH curve data at $1 <$ H

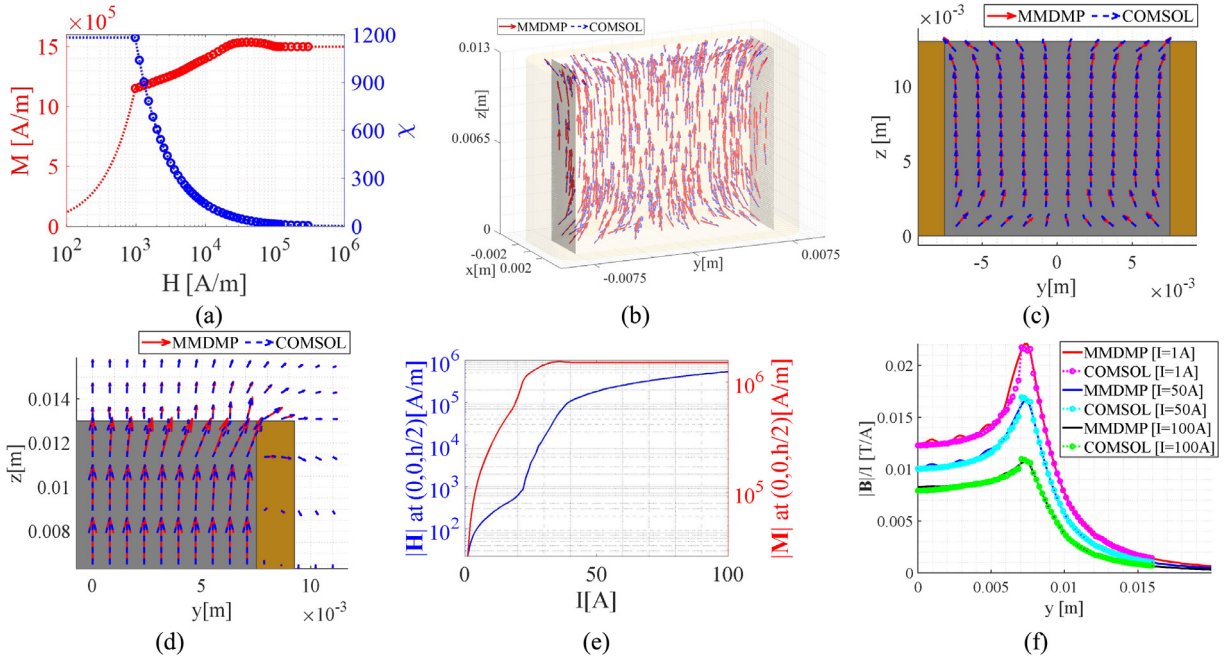


Fig. 7. Field of iron-core EM (a) MH curve and χ of core material, (b) $\mathbf{M}_{\mathrm{FM}}$ of the local sources with I = 50 A, (c) $\mathbf{M}_{\mathrm{FM}}$ at y–z plane with I = 50 A (d) $\mathbf{B}$ at y –z plane with I = 50 A, (e) $|\mathbf{M}_{\mathrm{FM}}|$ at the center of the core, (f) $|\mathbf{B}|/\mathrm{I}$ at $x = 0$ and $z = h + 0.5$ mm.

Table 3
Computational error of the MMDMP in Fig. 7(c–d).

Average computational error [%]			
M_y	M_z	B_y	B_z
2.4261	2.8370	0.6500	0.5263

(kA/m) $<$ 300 obtained from COMSOL. M and H are assumed to be linear at H (kA/m) $<$ 1 and constant at the saturation region.

Fig. 7(b) illustrates $\mathbf{M}_{\mathrm{FM}}$ at the barycenter of each local source. It is computed by the MMDMP and COMSOL. In Table 3, the computational errors of $\mathbf{M}$ and $\mathbf{B}$ are analyzed at the y-z plane illustrated in Fig. 7(c–d). In addition, the change of $\mathbf{M}_{\mathrm{FM}}$ is observed according to the current. Fig. 7(e) shows $\mathbf{M}_{\mathrm{FM}}$ at the center of the core, and it begins to be saturated near I = 40 A. This magnetic saturation limits the contribution of the iron-core. Therefore, in Fig. 7(f), $|\mathbf{B}|/\mathrm{I}$ decreases as current increases, even if $\mathbf{M}_{\mathrm{EM}}$ is not limited to current. This trend shows good agreement with the solution from COMSOL.

Force/torque between PM and iron-core EM

Force and torque interaction between the PM and the iron-core EM carrying 50 A current is investigated. The PM moves along the x-axis while keeping a 1 mm air-gap, as shown in Fig. 4. The PM is modeled with surface elements. The magnetization is assumed as $\mathbf{M}_{\mathrm{PM}} = \mu_0^{-1}\mathrm{B}_{rem}\mathbf{e}_z$, and the remanence B_{rem} is tabulated in Table 1. The iron-core is modeled with volume elements or surface elements according to whether the iron is nonlinear or not. The force $\mathbf{F} = \mathrm{F}_x\mathbf{e}_x + \mathrm{F}_y\mathbf{e}_y + \mathrm{F}_z\mathbf{e}_z$ and torque $\mathbf{T} = \mathrm{T}_x\mathbf{e}_x + \mathrm{T}_y\mathbf{e}_y + \mathrm{T}_z\mathbf{e}_z$ on PM are calculated by (38).

Fig. 8 illustrates each interaction force by $\mathbf{M}_{\mathrm{EM}}$ of the air-core EM and $\mathbf{M}_{\mathrm{FM}}$ of nonlinear iron-core. The advantage of the MMDMP is that it can compute the forces individually. On the other hand, FEM should generate lots of meshes at the media of the narrow gap between the core and current loops to separate the integral domain for the Maxwell stress tensor. The MMDMP only uses the independent models of the materials without the media, so the force contribution of each material can be analyzed more efficiently than FEM. In addition, the sum of both interaction forces from the MMDMP is compared to the solution from COMSOL. As summarized in Table 4, the MMDMP shows the remarkable computational speed with minor errors because there is no numerical integration

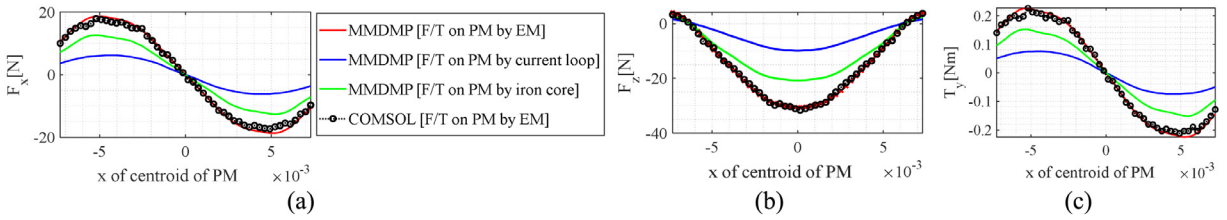


Fig. 8. Interaction force/torque between PM and nonlinear iron-core (a) F_x, (b) F_z, (c) T_y.

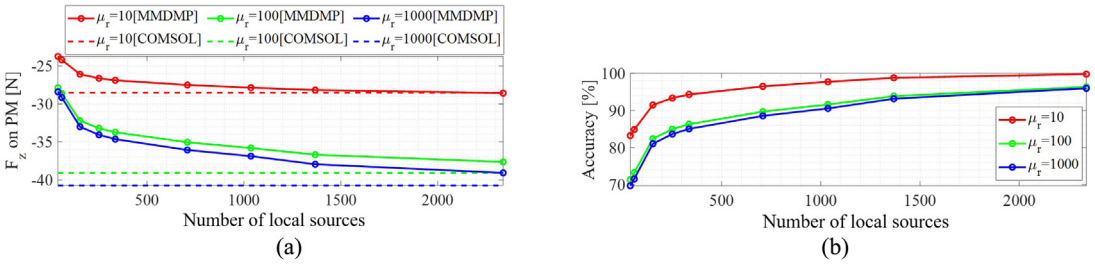


Fig. 9. Effect of the number of surface elements of the core and the permeability on the study of the interaction force (a) F_z, (b) Accuracy.

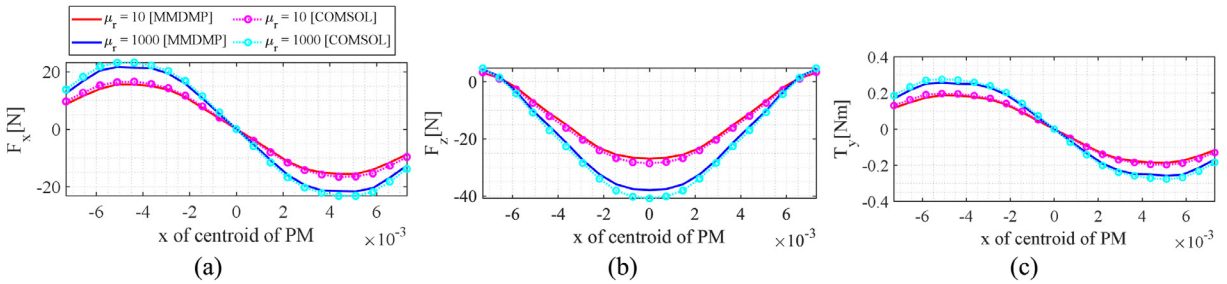


Fig. 10. Interaction force/torque between PM and linear iron-core (a) F_x, (b) F_z, (c) T_y.

in the whole computation. It is also because the MMDMP does not need substantial remeshing processes according to the location of the PM, generally required in FEM.

Figs. 9 and 10 illustrate the interactions assuming the iron-core is linear. Fig. 9 depicts F_z at the centroid of the PM, $x = 0$. It shows how the number of surface elements of the core can affect computation accuracy. Fig. 9(a) represents the results of computing F_z according to the number of elements and the relative permeability of the core μ_r. It shows that fewer elements are required for the lower permeability to satisfy a specific accuracy, as shown in Fig. 9(b). It is because higher permeability makes demagnetization tensors more dominant in (29). In other words, the geometry of the FM and the applied field distributions mainly affect the magnetic charge density on the material surface, so finer meshes are required. Fig. 10 illustrates the interaction according to the location of the PM for two different $\mu_r = 10$ and 1000. 336 surface elements of the core are utilized for $\mu_r = 10$ and 1368 for $\mu_r = 1000$, respectively. Both results show similar computational error, but computation for $\mu_r = 1000$ takes longer than 10. However, the MMDMP is still much faster than COMSOL, as shown in Table 4.

3.2. Analysis of the BLDC motor

A BLDC motor is analyzed to demonstrate the computational efficiency and accuracy of the MMDMP. Fig. 11 shows the rotor with the PMs and back iron and iron stators with air-core EMs. It is better to analyze the BLDC motor with a 3D model but it would take huge memory for $\mathbf{N}_V$ in (22) due to the geometric complexity of the iron-core. In addition, without loss of generality, it is commonly approximated in 2D model considering the symmetry.



(a) (b) (c)

Fig. 11. BLDC motor (a) Back iron and PM array, (b) Iron-core, (c) Assembly with winding.

Table 4
Computational performance of MMDMP in Figs. 8 and 10.

Figure		Average computational time [s]		Average computational error [%]		
Fig. 8		COMSOL	MMDMP	F_x	F_z	T_y
		55164	178	2.5440	1.8805	3.8430
Fig. 10	μ_r	COMSOL	MMDMP	F_x	F_z	T_y
	10	4612	39	2.5350	3.1507	4.4299
	1000	5583	132	2.6877	3.1251	4.9274

Table 5
Properties of the BLDC motor.

PM type	NdFeB (N42UH)	PM remanence	1.31T
PM/yoke/back-iron thickness	3/3/1.5 mm	Radius of stator and rotor	68.75/74.15 mm
Height	15 mm	Air-gap	0.5 mm
Number of poles/slots/turn	42/36/5	Core and back-iron material	Silicon steel NGO 35PN250
Winding type	Delta	Phase current	A(10A)/ B and C (5A)

The detailed geometric and electric/magnetic properties of the motor are listed in Table 5. The magnetic field and the torque of the rotor are analyzed in three steps. Firstly, the PM and the air-core EM array are modeled to compute the applied field to the iron parts $\mathbf{H}_0$. Then, the magnetization $\mathbf{M}$ of the iron parts is iteratively computed. Finally, the air-gap flux density and the interaction torque are calculated. The results are compared to the COMSOL, and the torque is further verified experimentally. The performance results, including accuracy and computation efficiency, are summarized in Table 6.

Fig. 12(a) illustrates the volume elements for the iron parts and approximated monopoles for the PM and EM arrays. In Fig. 12(b), COMSOL decomposes the iron parts more finely than the MMDMP because COMSOL should model the media region, requiring lots of meshes, especially in the air-gap. Fig. 12(c–d) shows that the χ fields from both methods match each other. The magnetic characteristics of the iron parts are described well, such as magnetic saturation at the back iron, the magnetization of the core by the phase current, and the magnetization of stator shoes according to the placement of the PMs. The computational error of the $\mathbf{M}$ field, obtained by the linear interpolation of $\mathbf{M}$ at the barycenter of each volume element, is about 7%. In Fig. 13, the $\mathbf{B}$ field at the middle of the air-gap is further calculated.

The torque model is further verified by experimental results using the torque measurement system consisting of the rotational stage and the torque sensor shown in Fig. 14(a). Fig. 14(b) depicts a torque on the rotor according to its mechanical angle. The MMDMP and COMSOL have a similar amount of error based on experimental results. The minor errors in both simulations are primarily attributed to errors in modeling 3D materials in the 2D space.

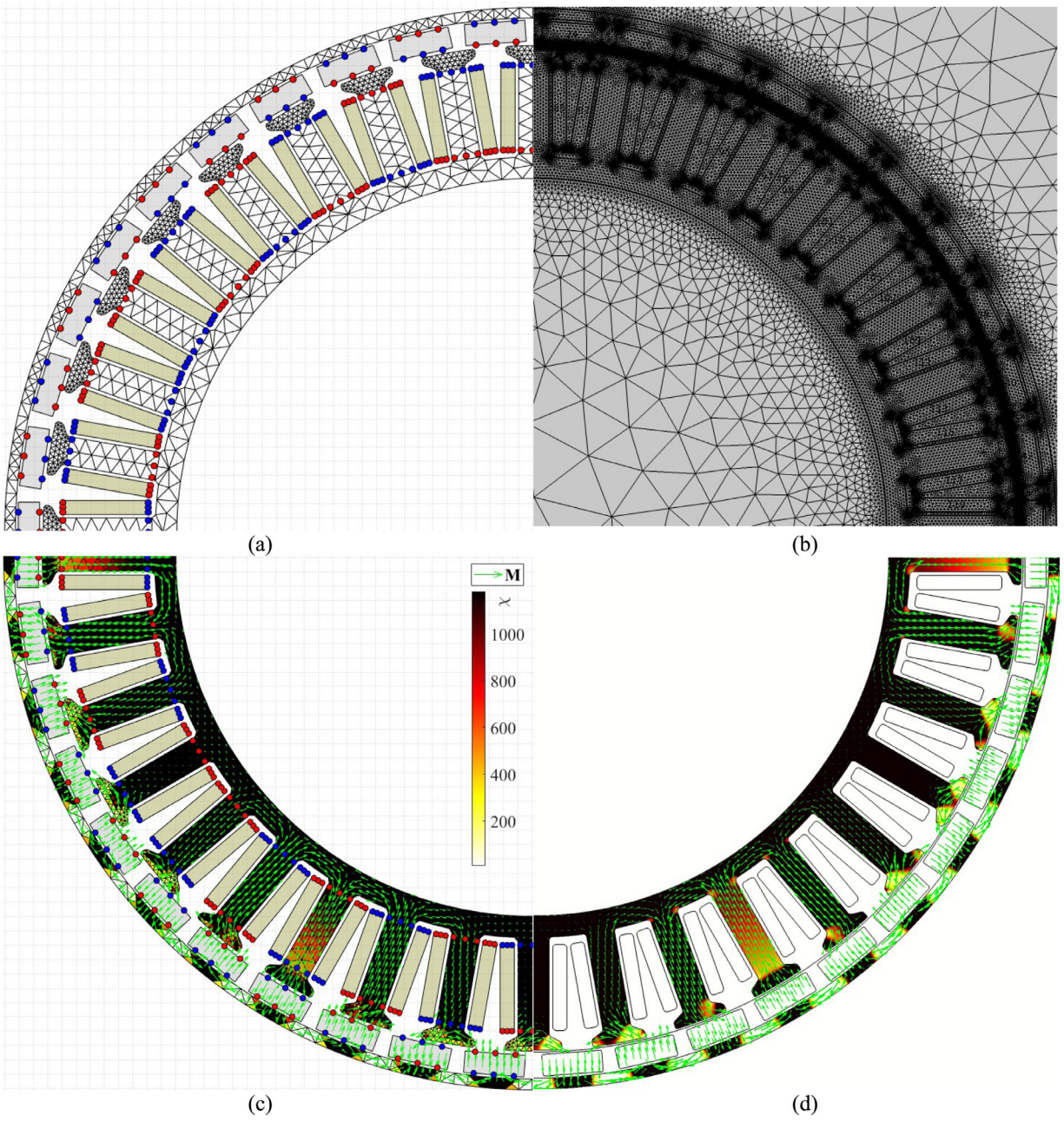


Fig. 12. Comparative studies of the BLDC between the MMDMP and COMSOL. (a) Local sources for the MMDMP, (b) meshes for COMSOL, (c) **M** and χ [MMDMP], (d) **M** and χ [COMSOL].

4. Conclusion

The MMDMP as a generalized magnetic source modeling method was developed for precise and fast computation of the magnetic field and force formulated as the sum of the closed-form solutions accounting for the magnetic effect of the surface and the volume elements. The demagnetization tensor was derived to compute the magnetic field by each element with its magnetization. The elements could be further approximated as a single pole for computational efficiency. Magnetic monopoles were utilized for the surface elements composing the PM, EM, and linear FM. Meanwhile, magnetic dipoles were located inside the volume elements of the nonlinear FM. Furthermore,

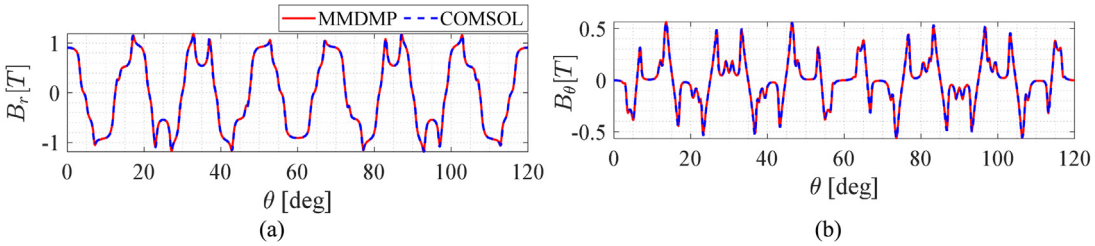


Fig. 13. B at **r** = 0.069 m·[cos θ, sin θ] (the middle of the air-gap) (a) B_r, (b) B_θ.

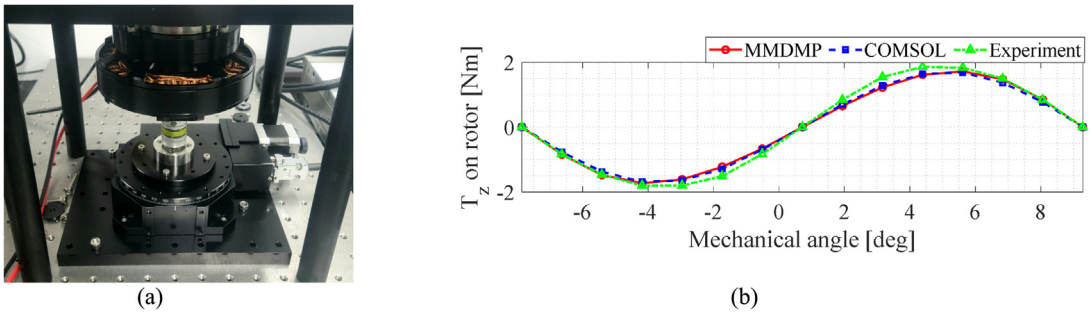


Fig. 14. Torque simulation and experiment of BLDC motor (a) Experimental setup (b) Torque on the rotor.

Table 6
Computational performance in Figs. 12c, 13 and 14b.

Average field computational error [%]			
M_x	M_y	B_r	B_θ
7.1209	7.1855	0.8186	0.8856
Computational time in torque computations [s]			
COMSOL		MMDMP	
9195		2034	
Average torque computational error based on the experiment [%]			
COMSOL		MMDMP	
6.3532		5.8990	

the magnetization of the FM and EM was analyzed to apply the MMDMP for both materials. Finally, two practical examples were demonstrated to verify the accuracy and computational efficiency of the MMDMP. The results were compared to the FEM and experiments. It is expected that the MMDMP method has the potentials for fast studying the design and control of electromechanical systems.

Declaration of competing interest

The authors declare that they have no known competing financial interests or personal relationships that could have appeared to influence the work reported in this paper.

Acknowledgments

This work was supported in part by the National Research Foundation of Korea (NRF) grant funded by the Korea government (MSIT) (No. 2020R1F1A1075857), and Basic Science Research Program through the National Research Foundation of Korea (NRF) funded by the Ministry of Education (No. 2020R1A6A1A03040570), respectively.

References

[1] F. Rogier, J. Segre, Mixed finite element method applied to a magnetostatic problem, Comput. Methods Appl. Mech. Engrg. 94 (1992) 1–11.

[2] M. Kuhn, The application of coupled BEFE formulations in technical magnetic field computations, Comput. Methods Appl. Mech. Engrg. 157 (1998) 193–204.

[3] J.S. Choi, J. Yoo, Structural optimization of ferromagnetic materials based on the magnetic reluctivity for magnetic field problems, Comput. Methods Appl. Mech. Engrg. 197 (2008) 4193–4206.

[4] S. May, M. Kästner, S. Müller, V. Ulbricht, A hybrid IGAFEM/IGABEM formulation for two-dimensional stationary magnetic and magneto-mechanical field problems, Comput. Methods Appl. Mech. Engrg. 273 (2014) 161–180.

[5] J. Chovan, C. Geuzaine, M. Slodič cka, A–ϕ formulation of a mathematical model for the induction hardening process with a nonlinear law for the magnetic field, Comput. Methods Appl. Mech. Engrg. 321 (2017) 294–315.

[6] Z. Bontinck, J. Corno, S. Schöps, H. de Gersem, Isogeometric analysis and harmonic stator-rotor coupling for simulating electric machines, Comput. Methods Appl. Mech. Engrg. 334 (2018) 40–55.

[7] K.M. Lee, H. Son, Distributed multipole model for design of permanent-magnet-based actuators, IEEE Trans. Magn. 43 (2007) 3904–3913.

[8] J. Lim, K.M. Lee, Distributed multilevel current models for design analysis of electromagnetic actuators, IEEE/ASME Trans. Mechatronics 20 (2015) 2413–2424.

[9] P. Elleaume, O. Chubar, J. Chavanne, Computing 3D magnetic fields from insertion devices, Proc. IEEE Part. Accel. Conf. 3 (1997) 3509–3511.

[10] K.M. Lee, K. Bai, J. Lim, Dipole models for forward/inverse torque computation of a spherical motor, IEEE/ASME Trans. Mechatronics 14 (2009) 46–54.

[11] H. Son, K. Bai, J. Lim, K.M. Lee, Design of multi-DOF electromagnetic actuators using distributed multipole models and image method, Int. J. Appl. Electromagn. Mech. 34 (2010) 195–210.

[12] W. Fang, H. Son, Optimization of measuring magnetic fields for position and orientation tracking, IEEE/ASME Trans. Mechatronics 16 (2011) 440–448.

[13] K. Bai, K.M. Lee, Direct field-feedback control of a ball-joint-like permanent-magnet spherical motor, IEEE/ASME Trans. Mechatronics 19 (2014) 975–986.

[14] K. Bai, K.M. Lee, J. Lu, A magnetic flux model based method for detecting multi-DOF motion of a permanent magnet spherical motor, Mechatronics 39 (2016) 217–225.

[15] J. Jeon, H. Son, Active control of magnetic field using eDMP model for biomedical applications, IEEE/ASME Trans. Mechatronics 23 (2018) 29–37.

[16] C.Y. Lin, K.M. Lee, Y.L. Chen, S.C. Huang, Distributed current source method for modeling magnetic and eddy-current fields induced in biological object, IEEE/ASME Trans. Mechatronics 23 (2018) 1038–1049.

[17] M. Li, K.M. Lee, Machine perception based on eddy current for physical field reconstruction of conductivity and hidden geometrical features, IEEE Trans. Ind. Informatics 15 (2019) 5392–5403.

[18] B. Hao, K.M. Lee, I. Chang, Magnetic machine perception for reconstruction of nonuniform electrical conductivity based on eddy current model, IEEE/ASME Trans. Mechatronics 25 (2020) 2318–2329.

[19] B. Hao, K.M. Lee, K. Bai, Distributed current source modeling method for 3D eddy current problem in magnetic conductor with discrete state-space J-φ formulation, J. Comput. Phys. 401 (2020) 109027.

[20] O. Chadebec, J.L. Coulomb, F. Janet, A review of magnetostatic moment method, IEEE Trans. Magn. 42 (2006) 515–520.

[21] V.P. Bui, O. Chadebec, L.L. Rouve, J.L. Coulomb, Noninvasive fault monitoring of electrical machines by solving the steady-state magnetic inverse problem, IEEE Trans. Magn. 44 (2008) 1050–1053.

[22] M. Forbes, W.S.P. Robertson, A.C. Zander, J.J.H. Paulides, Boundary-free analytic magnetic field calculations including soft iron and permanent magnets using an iterative discretization technique, IEEE Trans. Magn. 57 (2021) 2–6.

[23] R.I. Joseph, E. Schlömann, Demagnetizing field in nonellipsoidal bodies, J. Appl. Phys. 36 (1965) 1579–1593.

[24] K. Tang, H.W. Zhang, Q.Y. Wen, Z.Y. Zhong, Demagnetization field of ferromagnetic equilateral triangular prisms, Phys. B Condens. Matter. 363 (2005) 96–101.

[25] K.K. Nielsen, A.R. Insinga, R. Bjørk, The stray- and demagnetizing field from a homogeneously magnetized tetrahedron, IEEE Magn. Lett. 10 (2019).

[26] J.D. Jackson, Classical Electrodynamics, Wiley, New York, 1999.